35th Symposium on Naval Hydrodynamics
Nantes, France, 8 July - 12 July 2024

# The influence of boundary-layer thickness on incipient and developed cavitation in tip-leakage flow

P. S. Russell, K. Takahashi, L. Barbaca, J. A. Venning, B. W. Pearce & P. A. Brandner
(Australian Maritime College, University of Tasmania, Australia)

## ABSTRACT

The influence of boundary layer thickness on incipient and developed cavitation in a stationary tip leakage flow is investigated experimentally in a cavitation tunnel. Tests were conducted at a constant hydrofoil incidence of $6^{\circ}$ and fixed chord based Reynolds number of $3 \times 10^{6}$. The cavitation number was varied between 8 and 2 and the tip gap between 0.1 to 2 hydrofoil thicknesses. Four boundary layer values ranging from 0.3 to 2.1 hydrofoil thicknesses were tested. These thicknesses were achieved using a combination of streamwise position change and a boundary layer manipulation via an array of orifices using transpiration or ingestion. The 3D leakage vortex trajectory, overall sound pressure, and incipient event rate were measured for the above noted parameter space. Refinement of a robust method to capture the incipient event rates was required due to the large differences in its character as cavitation develops throughout this parameter space. Variation of boundary layer thickness was found to have little influence on the mean leakage vortex trajectory relative to the hydrofoil. Although, there was greater fluctuations in the instantaneous location due to additional turbulence with increasing boundary layer thickness. Overall sound pressure and incipient event rates typically increase from low values at the smallest gap to a maximum between about 0.6 to 0.8 hydrofoil thicknesses and then decrease with further gap increase to similar low initial values for all boundary layer thicknesses. Peak overall sound pressure and incipient event rates are greatest for the thinnest boundary layer and decrease with increasing thickness. These quantities do tend to converge for the thickest boundary layers suggesting that further increase would have little effect. Further experiments with thicker boundary layers are required to test this inconclusive observation.

## INTRODUCTION

Tip-Leakage Flow (TLF), i.e. the flow in the gap between the tip of a rotating blade and a static casing, is a feature observed in many fluid mechanics applications, most prominently in axial turbomachinery and ducted propulsors. Due to the complexity of the flow through the gap and a high blade-tip velocity, TLF is often a flow feature with the global pressure minimum, and consequently highest cavitation susceptibility.

Complex topology of TLF provides variety of features that may act as sites for cavitation inception, however, for a well designed tip geometry a global pressure minima is most likely to occur in the tip leakage vortex (TLV). While this premise may be true when the mean pressure field is considered, cavitation inception is often observed in nominally weaker secondary structures of TLF. In particular, experimental studies using a rotating model at large Reynolds number report cavitation inception in the small vortical filaments originating from the tip trailing edge (Oweis & Ceccio, 2005) and the jetting shear layer on the suction side of the hydrofoil (Wu *et al.*, 2011).

While the mean pressure in the core of the secondary structures is higher than that in the core of TLV, interactions between the weaker vortical filaments and the TLV can lead to stretching of the filament core resulting in a sudden drop in the core pressure. Consequently, momentary pressure values in the cores of the secondary structures may decrease well below that in the core of the TLV, rendering secondary structures sites of the global pressure minima and the location of cavitation inception (Oweis & Ceccio, 2005; Chang *et al.*, 2012). This transient type of small-scale cavitation inception has been documented in axisymmetric jets (Gopalan *et al.*, 1999; Ran & Katz, 1994) as well as in plane shear layers (O'Hern, 1990) or behind a backward-facing step (Agarwal *et al.*, 2020; Allan *et al.*, 2023).

TLF is characterised by a multitude of interacting flow features which affect the inception of cavitation. Unbounded finite-span lifting surfaces generate trailing vortices due to spanwise flows near the tip driven by the pressure difference between the two sides of the hydrofoil. This reduces the lift generated in the vicinity of the tip, increases the drag of the blade, and provides a mechanism for the downstream transport of vorticity from the hydrofoil surface. The cores of these trailing vortices are characterised by high rotation rates and low pressures.

As confinement is introduced in the vicinity of the tip, and flow through the gap reduces, the pressure difference between the two sides of the hydrofoil increases (Boulon *et al.*, 1999). For small clearances, the leakage flow is suppressed, producing a more two-dimensional flow, higher lift, and a weaker trailing vortex. However, the difference in pressure increases the angle between the flow through the gap and the free-stream flow which may induce local separation at the trailing edge . It may also induce development of low-pressure areas at the leading edge and flow separation within the gap which promote cavitation.

Rounding of the edge on the pressure side of the hydrofoil tip can be utilised to mitigate flow separation and cavitation within the gap, however, it is often accompanied by increased shear on the foil suction side contributing vorticity to the TLV (Laborde *et al.*, 1997).

In order to reduce modelling complexity, single stationary hydrofoil analogies of multi-bladed rotating geometries have been explored both experimentally (Boulon *et al.*, 1999; Gopalan *et al.*, 2002; Higashi *et al.*, 2002; Dreyer *et al.*, 2014; Russell *et al.*, 2020*a*) and numerically (You *et al.*, 2006, 2007; Zhang *et al.*, 2015; Guo *et al.*, 2016). Although, many aspects of the flow are not captured with a single hydrofoil analogy, these approximations have proved to be a useful tool in exploring a number of flow features that are also observed in the rotating flows they emulate.

The main flow parameters influencing the TLF and consequently cavitation inception include the Reynolds number, tip gap clearance, incoming wall boundary layer and the water nuclei content. A large body of literature exist reporting on the effect of the former two, with recent works by Russell *et al.* (2020*a*,*b*, 2022, 2023) providing new insights into the effect of the water nuclei content on the dynamics of incipient and developed cavitation in TLF. In contrast to the other parameters, the effect of incoming boundary layer thickness on cavitation inception has received little attention.

The influence of the incoming wall boundary layer (BL) on TLF has been investigated mainly in the context of pressure losses and flow instabilities in compressor cascades (Wagner *et al.*, 1985*a*,*b*; Tian & Simpson, 2007*a*,*b*; Li *et al.*, 2016). While these provide insights into the the influence of BL on TLF topology, the design considerations of compressor stages limit the scope of reported studies to small gap clearances. Furthermore, the variation of BL is often achieved by use of a moving end-wall, with emulation of the rotational effects, such as shearing of the TLF due to relative motion between the tip and the casing, being the primary aim in such instances, and the effect of BL on TLF being of lesser interest. More recent numerical work by Zhang *et al.* (2022) provided some insight in the fundamental topology of the TLF under varying boundary layer conditions. From their observations two opposing phenomena pertinent to cavitation inception can be identified. Firstly, with an increase in the boundary layer thickness the average velocity of the flow through the gap reduces. This indicates a weaker tip-leakage vortex and reduced jetting on the suction side tip, suggesting a decrease in cavitation susceptibility of the TLF flow. In contrast, the second phenomenon, an increase in the size and strength of the turbulent structures ingested into the TLF, may contribute to an increase in cavitation susceptibility of the TLF as the interaction of these structures with the TLV may lead to momentary structure stretching and related large pressure fluctuations. The intent of the current experimental study is to provide insight into which of these phenomena has a dominant effect by examining cavitation inception in TLF for a single stationary hydrofoil analogy while varying the BL thickness.

## EXPERIMENTAL SETUP

The experiments were performed in the University of Tasmania variable pressure water tunnel. The tunnel test-section is $0.6 \times 0.6$ m square at the entrance, by 2.6 m long. The test-section ceiling is horizontal with the floor sloping 20 mm over the length to maintain nominally constant speed and a zero-stream-wise pressure gradient. The operating velocity and pressure are controlled independently, with ranges from 2 to 13 m/s and 4 to 400 kPa absolute, respectively. The tunnel volume is 365 $m^3$ and is filled with demineralised water. Optical access is provided through acrylic windows on each side of the test-section.

The test-section absolute pressure is measured, depending on the value, from high- or low-range Siemens Sitrans P absolute pressure transducers models 7MF4333-1FA02-2AB1 (range 0–130 kPa) and 7MF4333-1GA02-2AB1 (range 0–400 kPa), with an estimated precision of 0.13 and 0.48 kPa respectively, both are accurate to within 0.065%. The test-section velocity is measured from the calibrated contraction differential pressure. Depending on the value, either low- or high-range Siemens Sitrans P differential pressure transducers models 7MF4333-1DA02-2AB1-Z (range 0–25 kPa) and 7MF4333-1FA02-2AB1-Z (range 0–160 kPa) are used, with estimated precision of 0.007 and 0.018 m/s respectively. The test section velocity has been measured to be spatially uniform to within 0.5%, has a temporal variation of less than 0.2%, and a free stream turbulence intensity of 0.5%. The water dissolved gas content is measured using an Endress+Hauser OxyMax WCOS 41 membrane sensor. Further details on the facility can be found in Brandner *et al.* (2006, 2007).

The experimental setup has been developed to study cavitation in the gap flow between a stationary hydrofoil and the ceiling of the tunnel test-section, as schematically represented in Figure 1. The hydrofoil and mounting block are made out of a single forged stainless steel billet. The hydrofoil has a chord of $c = 280$ mm, and the span can be varied between $s = 540$ mm and 600 mm. The use of a NACA 66-012 mod section analogy at the tip, results with a tip thickness, $t = 33.6$ mm. To suppress the flow separation and delay the onset of the gap cavitation, fairing is applied to the tip of the hydrofoil Russell *et al.* (2023). The hydrofoil tapers towards the root, with the maximum root thickness of 67.2 mm. A 90 mm long parallel section is added between the hydrofoil root and the mounting block to ensure a streamlined flow along the foil/wall junction as the foil is traversed in the vertical direction. The mounting block is a 290 mm long $\times$ 100 mm wide $\times$ 605 mm high prism housed within the traversing assembly.

The traversing assembly allows for a continuous adjustment of the tip gap ($h$) and the incidence ($\alpha$) of the hydrofoil. For the present work the gap was adjustable in the range $1 \leq h \leq 70$ mm and the incidence in the range $-10^\circ \leq \alpha \leq 10^\circ$. The gap and the incidence adjustments were controlled using Tolomatic 32RSA-HT1 stepper motor electric linear actuators, driven by a Tolomatic ACS stepper driver motor controller, with a maximum thrust of 18.5 kN. The actuators have an accuracy of 0.01 mm across a 300 mm travel.

Experiments were performed for four boundary layer thicknesses $\delta_{99} = 10, 20, 30 \,\&\, 70$ mm. The two intermediate $\delta_{99}$ values were for a natural boundary layer developed over the test-section ceiling, with the hydrofoil model leading edge located 0.7 m and 1.9 m downstream from the test-section entrance (Figure 1).

The two extreme $\delta_{99}$ values were obtained using a boundary layer control system (Figure 1), with a working principle based on injection or ingestion of water through a penetration fitted with a perforated plate located upstream of the test-section entrance (as described in Belle *et al.* (2016)). A thinned boundary layer ($\delta_{99} = 10$ mm) was achieved via ingestion of boundary layer liquid through a perforated plate with an array of $422 \times 10$ mm diameter holes, with a 12 mm spacing between the holes in streamwise direction and 14 mm spacing in spanwise direction (designated as 'plate $f$' in Belle *et al.* (2016)), and the hydrofoil located in the upstream location along the test-section. A thickened boundary layer ($\delta_{99} = 70$ mm) was achieved via injection of transverse jets into the boundary layer through a perforated plate with five rows of holes in a triangular configura-

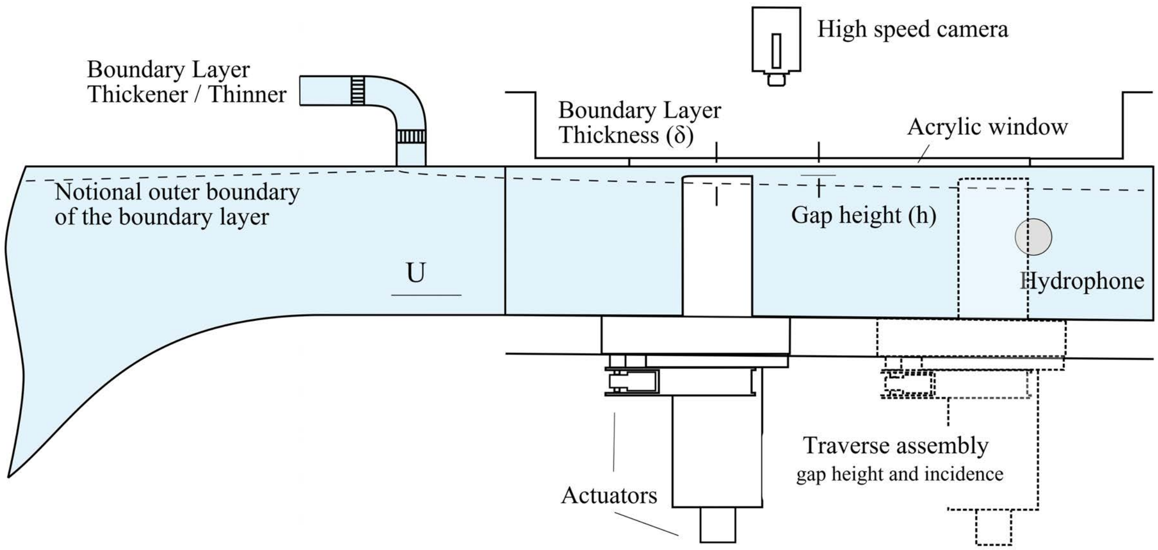


**Figure 1.** A schematic of the hydrofoil model mounted in the tunnel test section via a traverse assembly. The boundary layer thickness ($\delta$) is adjusted via mass ingestion and transpiration upstream. Tip gap clearance ($h$) and incidence of the hydrofoil ($\alpha$) can also be adjusted.

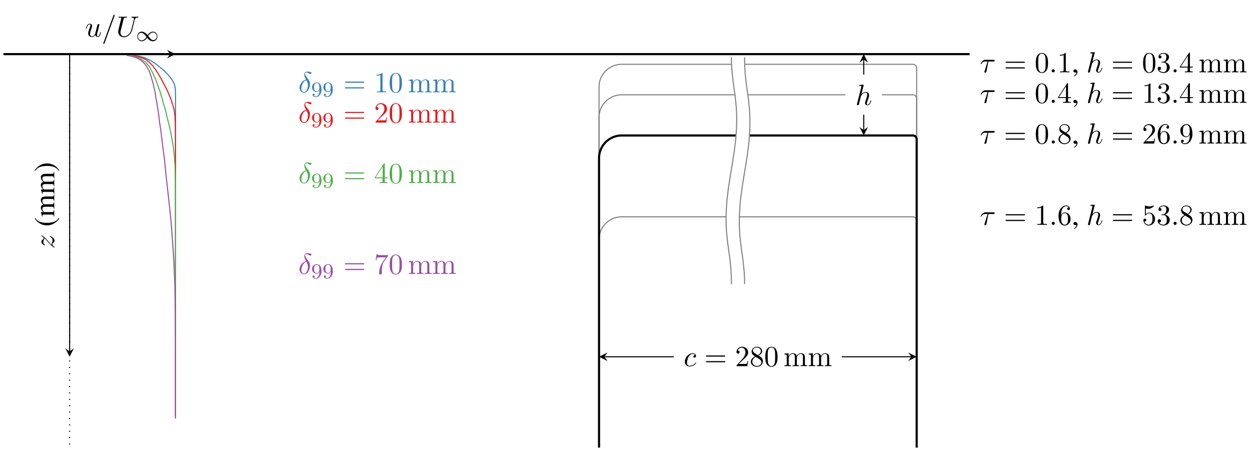


**Figure 2.** A schematic showing the scale of the boundary layers in relation to some of the tip gap clearance tested. The nominal boundary layer profiles are plotted from prior pitot tube measurements (Smith *et al.*, 2021; Belle *et al.*, 2016). The bold hydrofoil outline depicts a gap height $\tau = 0.8$.

tion, increasing in diameter in downstream direction (Smith *et al.*, 2021), and the hydrofoil located in the downstream location along the test-section. Boundary layer thickness is non-dimensionalised using the hydrofoil thickness ($\delta/t$), resulting in an investigated range $0.3 \leq \delta/t \leq 2.1$. A schematic summarizing the range of investigated boundary layer thicknesses and their scale compared to the range of the investigated tip gap clearances is presented in Figure 2.

High-speed imaging of the cavitation topology in the gap was acquired using two Phantom v2640 cameras with a maximum resolution of 2048 $\times$ 1952 pixels, mounted above the tunnel test section and to the side of the test section. The camera was equipped with a Nikon AF Nikkor 24 mm f/2.8 D lens with the images acquired at a cropped resolution of 2048 $\times$ 640 pixels at a sampling rate of 10000 frames per second. Continuous illumination was provided from two Effilux EFFI-BL-LITE-1M12P 650 $\times$ 650 mm LED panels mounted to the side of the test section and three Veritas Constellation 120 LED lamps mounted above and to the side of the test section. The image acquisition was controlled via Phantom PCC 3.4.4 software. Optical access to the gap was provided through a 1150 mm long $\times$ 215 mm wide acrylic window in the test section ceiling for the hydrofoil in the upstream location and a 1020 mm long $\times$ 350 mm wide acrylic window in the test section ceiling for the hydrofoil in the downstream location.

Acoustic measurements were obtained using a Brüel & Kjær Type 8103 hydrophone (voltage sensitivity 25.1 $\mu$V/Pa) mounted in a flooded cavity (kept at the same pressure as the tunnel test section) beneath a 10 mm polyurethane diaphragm, with a 149 mm sensing diameter (Doolan *et al.*, 2013). The hydrophone was mounted in the side wall, 150 mm below the ceiling and 2.1 m from the entrance of the test section. The signal was conditioned using a Brüel & Kjær Nexus conditioner and amplifier, which was also used to apply a 0.1 Hz - 100 kHz bandpass filter. The filtered signal was acquired using a National Instruments PXIe-4497 card at a sampling rate of 204.8 kS/s. Each acoustic measurement was performed for a period of 60 s.

The high-speed imaging and the acoustic measurements were triggered independently, however, the data was synchronized by recording the camera trigger signal along with the acoustics and using it to align the two datasets. The camera was operated with a post trigger, so that once an incipient event was manually observed or heard, the camera trigger was activated.

All the experiments were performed for the hydrofoil chord-based Reynolds number, $Re = Uc/\nu = 3 \times 10^6$, where $U$ $(m/s)$ is the mean flow velocity and $\nu$ $(m^2/s)$ is the water kinematic viscosity, and the hydrofoil incidence $\alpha = 6°$. The hydrofoil tip gap clearance was non-dimensionalised by the maximum thickness of the hydrofoil tip section, $\tau = h/t$, with an investigated range $0.1 \leq \tau \leq 2$.

The cavitation number is defined as $\sigma = (p-p_v)/0.5\rho U^2$, where $p$ $(Pa)$ is the static pressure at the tunnel ceiling, $p_v$ $(Pa)$ is the water vapour pressure and $\rho$ $(kg/m^3)$ is the water density. The experiments were performed for a range of $\sigma$ values $2 \leq \sigma \leq 8$. For $\sigma \leq 4$ sporadic cavitation in the cross-flow jets of the BL control system was observed. In order to avoid ambiguity related to potential contamination of the tunnel natural nuclei population with the cavitation products the data obtained for $\sigma \leq 4$ are not presented.

The experiments were performed using the natural nuclei population present within the tunnel under de-gassed conditions. The tunnel natural nuclei population was characterised by Khoo *et al.* (2020) using measurements acquired via mechanical activation in a Cavitation Susceptibility Meter (CSM). Khoo *et al.* (2020) demonstrated that this population is practically invariant to tunnel operating conditions for dissolved oxygen levels below 4 ppm. Current experiments were performed with a dissolved $O_2$ content between 2.75 and 3.5 ppm.

## RESULTS AND DISCUSSION

### Acoustic event detection algorithm

The characterisation of cavitation for different boundary layer thicknesses and gap heights was primarily performed through analysis of hydrophone data. To extract the event rate a re-design of method employed in the previous studies of Russell *et al.* (2022, 2023) was used. It was found that for the current measurements, a single incipient event would regularly trigger multiple event registrations. This was primarily due to the long lived nature of the acoustic signature the flow generates (see Figure 3). Unlike in cavitation susceptibility meter measurements — from which the original method was adapted — the large structures generated in leakage vortex regularly persist as they are advected downstream of the hydrofoil, producing noise. The slow diminution of the sound made localising the bounds of an event with thresholding difficult. To better understand the time-frequency content of the acoustic data, the wavelet transform was analysed for a range of flow conditions. A sample time series and its wavelet transform are presented in Figure 3.

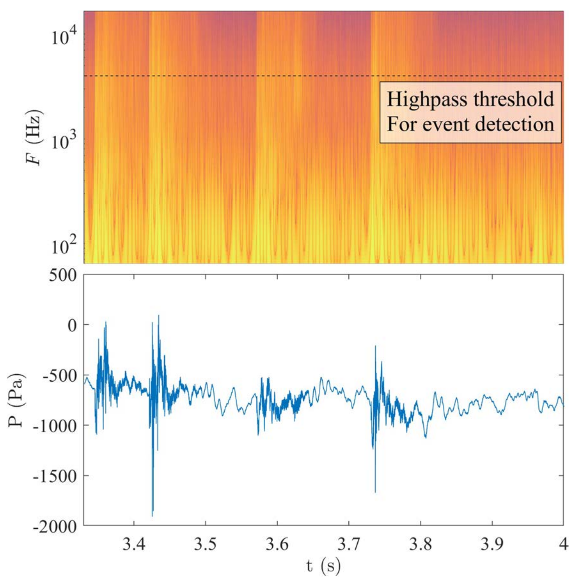


**Figure 3.** Wavelet and time series of hydrophone data for $\sigma = 4$ and boundary layer thickenss of $\delta_{99} = 30$ mm, $\alpha = 6°$, and $\tau = 0.4$.

Preference was given to localisation of the event in time so that a Degree Of Gaussian (DOG) mother wavelet was employed. The scaleogram with time suggests that the best contrast between the periods free of cavitation and those during incipient events is found for frequencies above 4 kHz.

Despite needing some changes in its execution a similar strategy to the previous event detection algorithm was taken, namely: high-pass filtering to isolate the relevant frequencies, rectification to work with one-sided information, smoothing and thresholding, and closure of small gaps in an otherwise contiguous event.

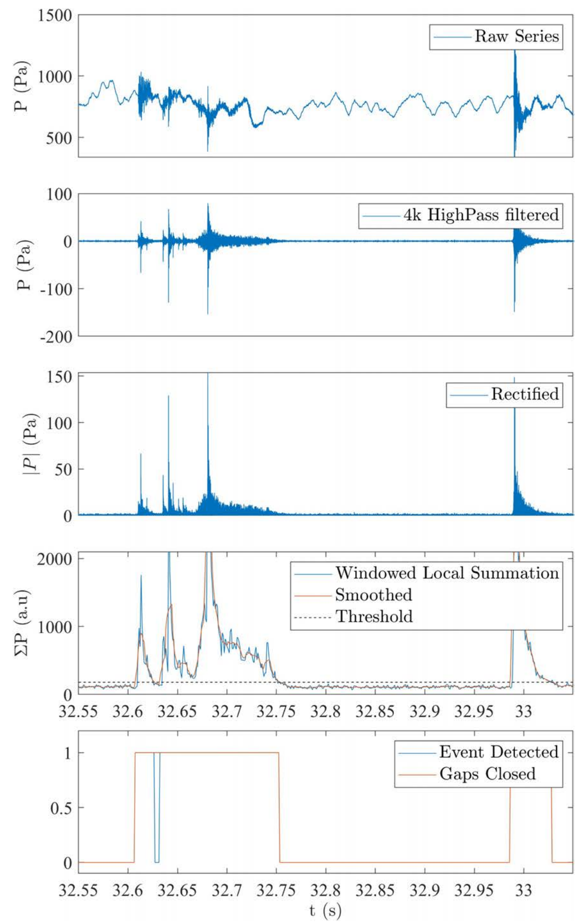


**Figure 4.** Outline of the event counting algorithm used to measure cavitation event rate. Plotted for boundary layer thickness of $\delta_{99} = 30$ mm, and $\alpha = 6°$, $\tau = 1$.

Previously low-pass filtering was used to smooth the rectified signal. The strength of nearby peaks caused the low-pass filter to introduce small oscillations so that when the mean signal strength approached the threshold value many threshold crossing occurred. This was mitigated by grouping closely spaced threshold crossings together, and could be helped by increase smoothing. Issues arose when the small scale, low amplitude incipient events close to inception are considered. The level of smoothing required would squash these event from registering.

To circumvent these issues a new approach was employed. Rather than low-pass filtering, the rectified signal was down-sampled by summation over a local window of 1 ms. Despite additional smoothing being applied after the downsampling, the effect was that the small scale events still exceeded the chosen threshold while the trailing edge of a larger events being advected downstream were smoothly represented. A visual outline of the process is presented in Figure 4.

**Comparison of incipient events for different boundary layer thicknesses.**

Differences in the signature of incipient events with increased boundary layer thickness were investigated by comparison of the simultaneously acquired high-speed imagery and hydrophone measurements. A series of four images from the high-speed data are presented for a boundary layer thickness of $\delta_{99} = 30$ mm in Figure 5, and $\delta_{99} = 70$ mm in Figure 6. Paired with these image sequences are the raw hydrophone data, along with the wavelet transform. Aside from boundary layer thickness the flow conditions were identical.

For this condition inception in the flow occurred in the leakage vortex just upstream of the trailing edge. The cavity rapidly grew downstream along the vortex core filling it with vapor. Its progress was just as suddenly slowed at a downstream location of approximately half a chord from the trailing edge. When viewed as a movie the cavity displays a momentary collapse and a mist of small bubbles is generated locally at the cavity trailing edge. After a brief pause, the cavity continues to grow downstream, but with a significantly reduced diameter. Eventually the leading edge of the cavity begins to be advected downstream.

These features are reflected in the acoustics data. The sudden pause in progress and generation of microbubbles corresponds to a sharp spike in acoustic pressure (see, Figure 5f). While the growth phase of the cavity and its advection downstream give rise to high-frequency fluctuations, they are overshadowed by the pressure spike. This initially cause difficulties in alignment of the two data sources as the most noticeable feature from the acoustic data occurred well after initial cavity growth. Proper alignment was resolved by recording the camera trigger signal as a second input alongside the acoustic data at the same sampling frequency of 204800 Hz.

The features of the both the high-speed and acoustic data are remarkably similar between the two boundary layers. The only noticeable difference in the images are a slight increase in the variability of the cavity along its trajectory with increased boundary layer thickness. The extension of this trend for other clearance height combinations are presented in Figure 7 and Figure 8.

**Vortex trajectories**

The 3D trajectory of the tip leakage vortex was captured by two high-speed cameras, that view the flow from above, and from the side of the test section. Selected still images from the high-speed data are presented for $\tau = 0.2, 0.6, 1.6$ and 2 and a boundary layer thickness of $\delta_{99} = 30$ mm and $\delta_{99} = 70$ mm in Figure 7. To visualise the leakage vortex the flow was seeded with a dense plume of polydisperse freestream nuclei for $\sigma = 3$. Cavitation and the accumulation of bubbles collected within the core of the tip leakage vortex reveals its 3D outline. To provide a sense of scale the location of $\delta_{99} = 30$ mm and $\delta_{99} = 70$ mm from the ceiling is superimposed on the images with a red dashed line in the side on view. For the small $\tau$ jetting within the gap pushes the leakage trajectory away from the suction face of the hydrofoil. When viewed from above the leakage vortex forms an almost straight line downstream from the near the leading edge of the model. From the side the vortex is deflected, beginning at a height the same as the gap, to a height roughly the same as the maximum thickness of the model. As it so happens this places the trajectory at a similar height to the boundary layer thickness for the $\delta_{99} = 30$ mm case. It now maintains a constant position in relation to the tip, located roughly 0.1 $z/C$ below the tip. As the gap widens the leakage vortex also rolls up closer to the model, pulling in towards the hydrofoil trailing edge. The vortex trajectory relative to the hydrofoil tip remains effectively unchanged with significant change in boundary layer thickness, as evident in Figure 7. This result suggests the global flow and vortex strength remains relatively unchanged and that the mass flux through the gap is not greatly

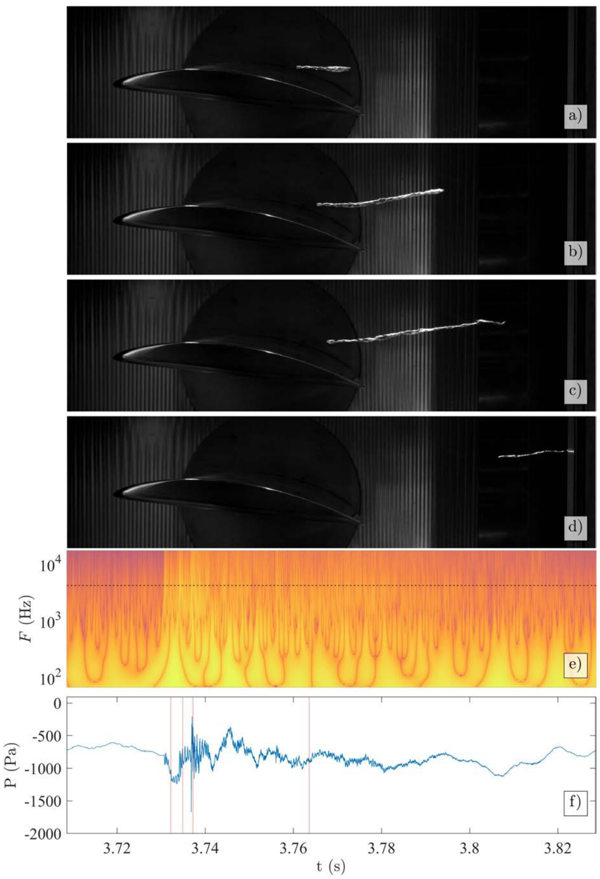


**Figure 5.** a-d) Images from high-speed data are presented along side concurrent hydrophone data for $\sigma = 4$ and boundary layer thickness of $\delta_{99} = 30$ mm, $\alpha = 6°$, and $\tau = 0.4$. e) Wavelet transform using a DOG mother wavelet of f) the raw acoustic data.

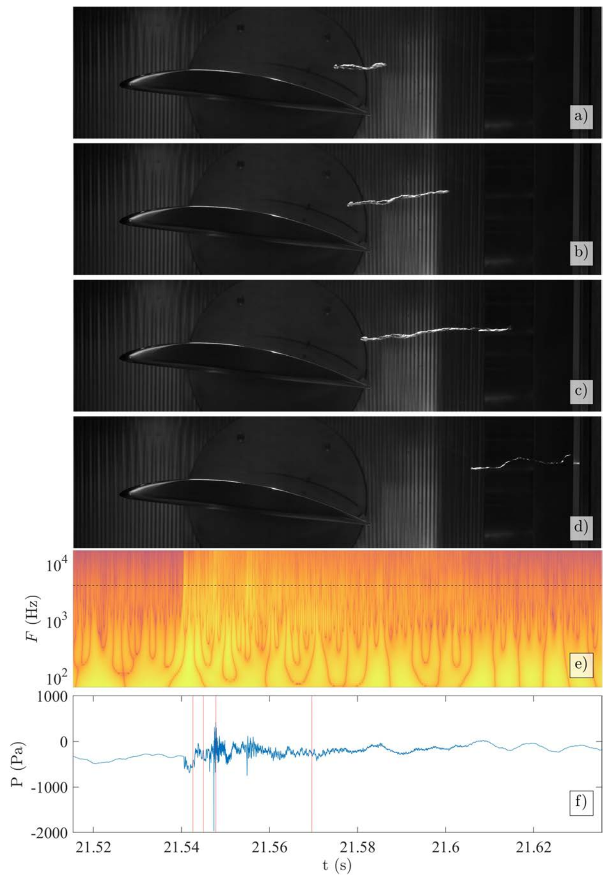


**Figure 6.** a-d) Images from high-speed data are presented along side concurrent hydrophone data for $\sigma = 4$ and boundary layer thickness of $\delta_{99} = 70$ mm, $\alpha = 6°$, and $\tau = 0.4$. e) Wavelet transform using a DOG mother wavelet of f) the raw acoustic data. These are the same conditions as in Figure 5

affected by the boundary layer thickness. This is arguably not unexpected given the relatively small change in displacement thickness.

The flow visualisation can also be used to consider the effects of boundary layer turbulence. The differences are predominately limited to the unsteadiness of the trajectory. This can be quantified through a heat-map of the vortex location, produced by retaining the maximum pixel intensity over successive frames from the high-speed video, see Figure 8. The increased width of the heat-map indicates that for $\tau = 0.2$ the vortex meanders over a region twice that of the thinner boundary layer case. This ratio reduces proportional to immersion of the tip inside the boundary layer. In summary the tip leakage vortex is more affected by turbulence than mass flux with change in boundary layer thickness.

**Incipient event rate with boundary layer**

The acoustic signature of cavitation inception has been quantified for varying boundary layer thickness and gap height using three parameters extracted from the acoustic data: over-all sound pressure level (OASPL) of the high-pass filtered data, acoustic event rate, and the proportion of time for which acoustic excitation related to cavitation was observed. These are plotted in Figure 9. Time averaged information about the flow is capture in the OASPL, plotted in the first column of the Figure 9 (a-e). The plots of OASPL are for the hydrophone data processed using the inbuilt high-pass filter function in MATLAB with a cut-off frequency of 4000 Hz. The data converge to similar background values for both small, and large $\tau$. Consistent with the previous results of Russell *et al.* (2023), a peak is observed for a gap height of between $\tau = 0.6$–$0.8$. The extensions to this result is that increasing the boundary layer thickness significantly reduces the strength of the peak. As the cavitation number is reduced and more of the leakage vortex falls below vapor pressure the discrepancy between the thin and thick boundary layer is reduced.

To probe whether the increase in OASPL was due to increased strength, frequency, or duration of acoustic excitation, the event rate was measured using the event detection algorithm previously described. The frequency of activations are plotted in the middle column of Figure 9 (f-j). They indicate that for small $\tau$ the low OASPL is due to infrequent cavitation in the leakage vortex. From Figure 8, increased jetting within the gap due to confinement does not overcome the decreased volumetric flow rate leading to a less coherent vortex of reduced strength. Consequently the incipient cavitation rates were also small. As $\tau$ and the leakage vortex strength is increased, so too did the incipient event rates. However, for large $\tau$ the gap was so wide that the leakage vortex effectively became an unbounded tip vortex, and reduced in strength. In general the OASPL increased in proportion to the incipient event rate. Gaps in the data for large boundary layers in Figure 9 f,g) are due to a complete lack of events across the 60 s sample when plotted on a logarithmic scale.

In addition to the event rate the proportion of the signal for which cavitation activity was detected was also analysed. The percentage of activity within the signal follows closely the overall event rate across each of the parameters, indicating that the duration of each event remains the same for comparable boundary layer thickness, gap heights, and cavitation number. This agrees with the comparisons made between Figure 5 and Figure 6 but shows that this conclusion can be generalised to the other combinations of flow parameters.

In summary the only modification to the flow is in the measured acoustic event rate as boundary layer thickness is increased. Vortex trajectories appear to be unchanged by boundary layer thickness increase although with greater variability due to turbulence. This suggest that the reduction in over-all pressure and event rate is due to turbulent breakup of the the leakage vorticies.

**Conclusion**

The influence of wall boundary layer thickness on incipient and developed cavitation of a stationary tip leakage flow has been investigated for several tip gaps, boundary layer thicknesses and cavitation numbers.

From detailed investigation of individual inception events it has been found that events in tip

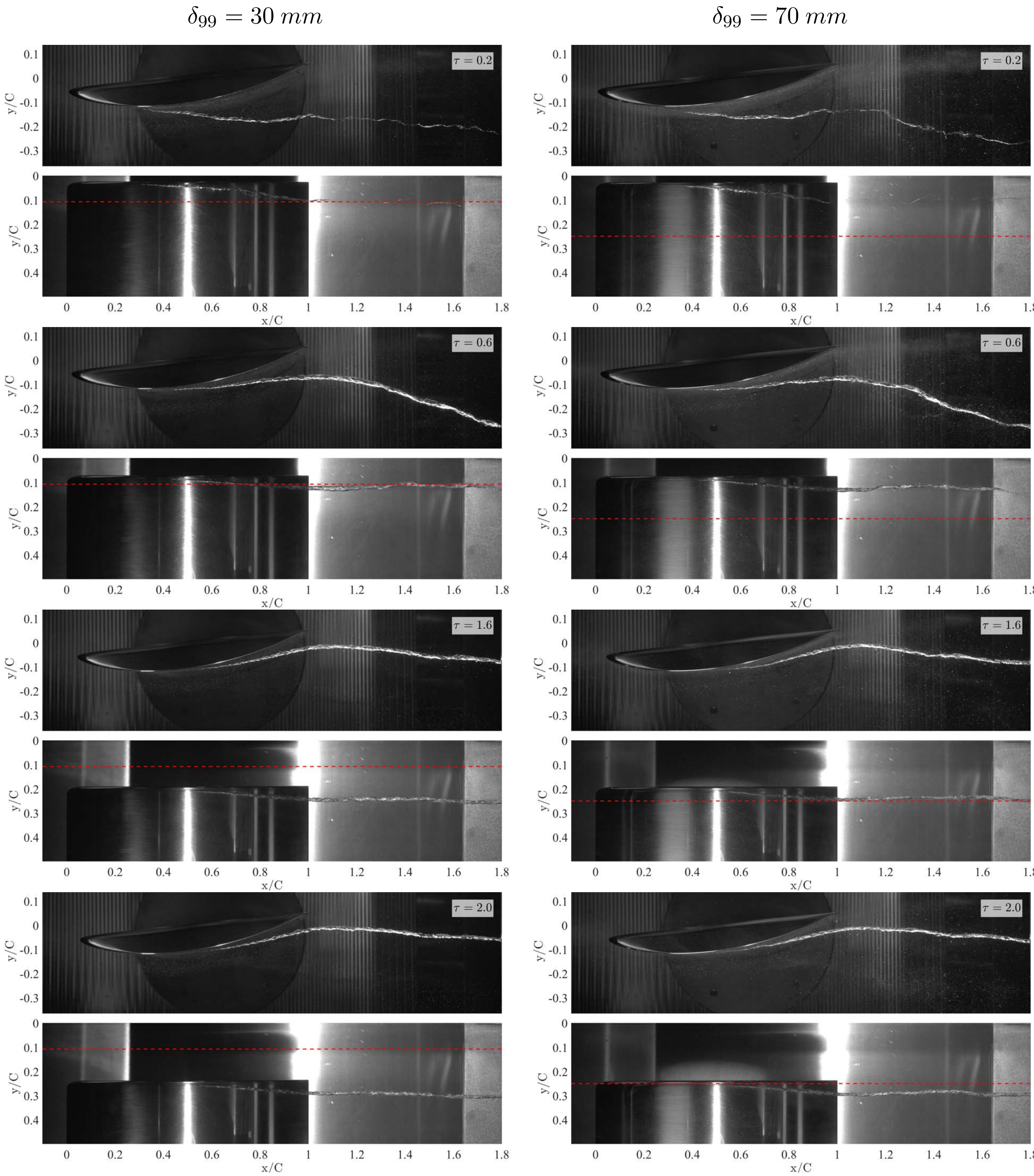


**Figure 7.** Instantaneous images of the leakage vortex trajectory for selected gap height and boundary layer thicknesses. Microbubble nuclei injection has been used aid visualisation for $\alpha = 6^{\circ}$. The red dashed line indicates the location of $\delta_{99}$ for the nominal boundary layer thickness under test.

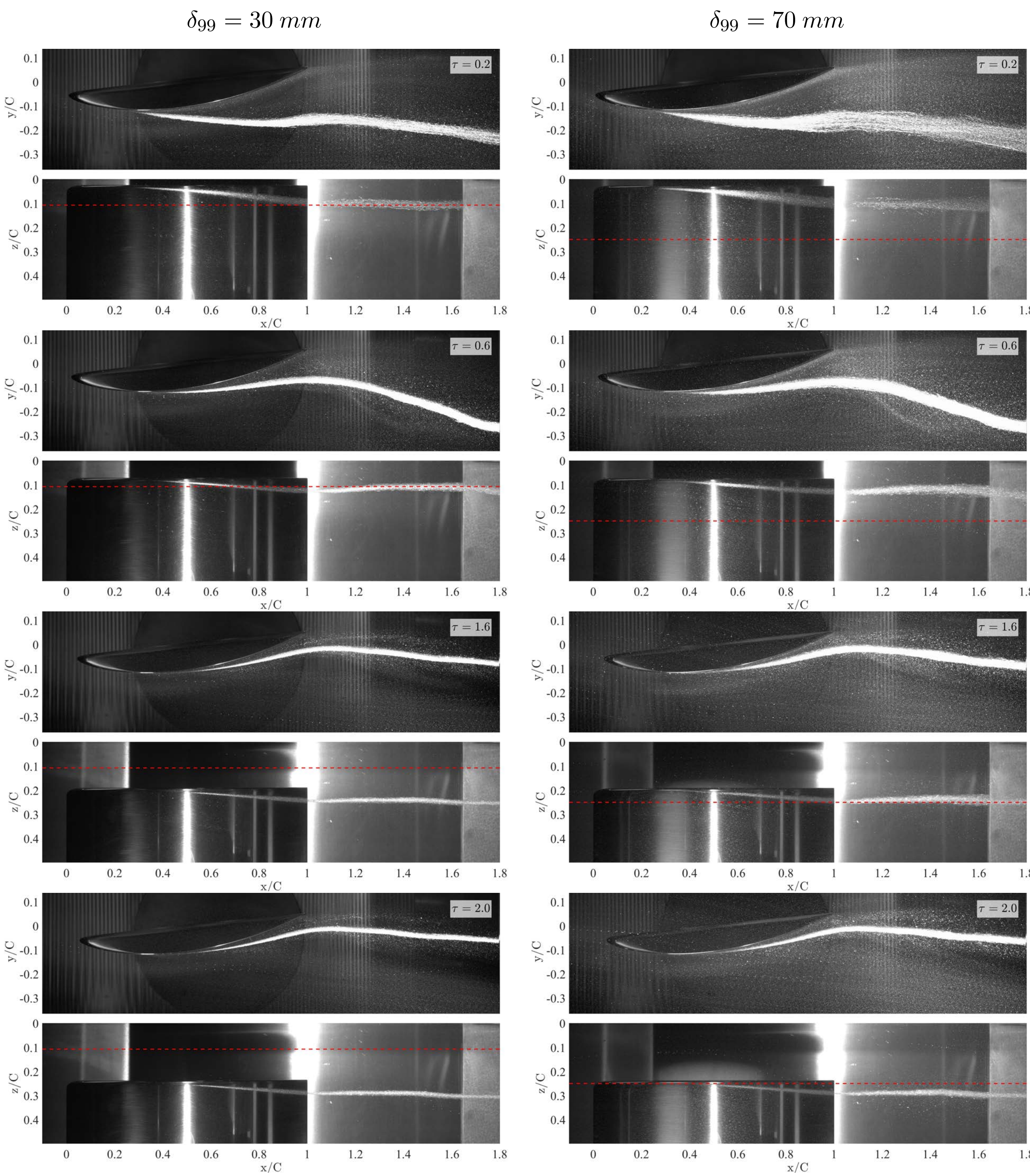


**Figure 8.** Superposition of 200 images to capture the variation of the leakage vortex trajectory for selected gap height and boundary layer thicknesses. Microbubble nuclei injection has been used aid visualisation for $\alpha = 6°$.

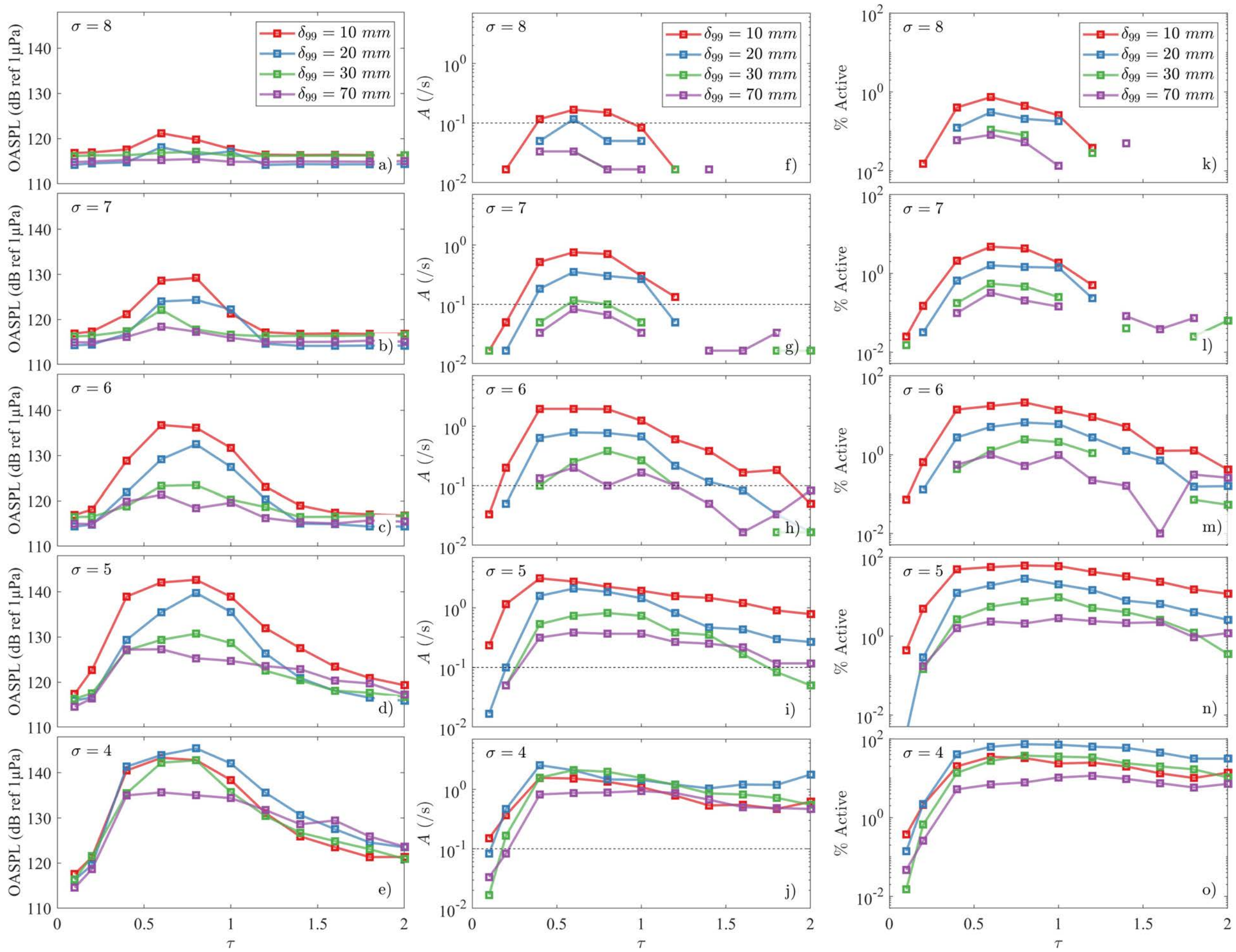


**Figure 9.** Measurements of acoustic events for $\alpha = 6^{\circ}$ for various boundary layers for conditions, gap heights ($\tau$), and cavitation numbers just below inception. a-e) Over-All Sound Pressure Level (OASPL) for the 4 kHz high-pass filtered data. f-j) Incipient event rate. k-o) Proportion of the acoustic recording where a cavity was detected, expressed as a percentage.

gap flows tend to be relatively long lived compared with other typical incipient events. This is due to the dynamics associated with their downstream advection. An improved algorithm for incipient event detection that eliminates false detections from a single event has been developed and applied to the present data set.

Examination of incipient events and visualisation of leakage vortex trajectories show that relatively large changes in boundary layer thickness have little effect on either. Incipient events show little difference either temporally or spatially and the vortex trajectories relative to the hydrofoil tip are essentially unchanged for 30 mm and 70 mm boundary layer thicknesses for all tip gap values investigated. Superposition of a large number of instantaneous images of visualised trajectories for various gaps and boundary layer thicknesses do reveal temporal variations in the trajectories. These results show that vortex trajectories have greater spanwise fluctuation downstream of the hydrofoil trailing edge for the thicker boundary layers compared with the thinner. This variation is presumably attributable to greater turbulence ingestion for the thicker boundary layers cases.

Significant differences do however occur in overall sound pressures and incipient event rates with change in boundary layer thickness. Inception commences with low event rates at a cavitation number of about 8 increasing in a power law with further reduction until saturation at about 4. Typically event rates and sound pressures increase by up to and order of magnitude from the smallest gaps to the peak values for gaps between 0.6 to 0.8 reflecting the largest velocities or vortex strengths. The thinnest boundary layers showed the greatest overall sound pressures and event rates. Event rates decrease with increasing boundary layer thickness. For the range of thicknesses investigated these initially decreased with increasing boundary layer thickness, tending to converge for the thickest boundary layers. This suggest that further increase may have little effect, requiring future tests in thicker boundary layers. For incipient cavitation numbers over-all sound pressure and event rates tend to decrease with further increase in gap height back to low values similar to those for the smallest gap. For lower cavitation numbers where event rates become large the rates and sound pressure don't return to the initially small values as more of the vortex becomes susceptible.

These results would imply that mass flux associated with the bulk tip leakage flow are little affected by boundary layer thickness i.e. due to relatively small change in displacement thicknesses compared with gap height. Turbulence levels however, do have a significant effect as revealed in fluctuations of the tip leakage vortex trajectory and significant changes in event rates and overall sound pressures. These would seem attributable to turbulent fluctuations disrupting the combined strength of the tip leakage vortex coherence.

## Acknowledgements

This project was supported by the US Office of Naval Research and ONR Global through NICOP S&T Grant no. N62909-19-1-2062, and the 2019 U.S. Multidisciplinary University Research Initiative (MURI) and the Australian Defence Science and Technology Group (DSTG). The authors are grateful for the technical assistance provided by Mr. Steven Kent and Mr. Robert Wrigley when conducting these experiments.

## References

Agarwal, K., Ram, O., Wang, J., Lu, Y. & Katz, J. 2020 Measuring the 3D pressure field and relating it to cavitation inception in a turbulent shear layer. In *33rd Symposium on Naval Hydrodynamics*.

Allan, E. S. C., Barbaca, L., Veninng, J A., Russell, P. S., Pearce, B. W. & Brandner, P. A. 2023 Nucleation and cavitation inception in high reynolds number shear layers. *Physics of Fluids* **35** (1).

Belle, A., Brandner, P. A., Pearce, B. W., de Graaf, K. L. & Clarke, D. B. 2016 Artificial thickening and thinning of cavitation tunnel boundary layers. *Experimental Thermal Fluid Science* **78**, 75–89.

Boulon, O., Callenaere, M., Franc, J. & Michel, J. 1999 An experimental insight into the effect of confinement on tip vortex cavitation of an elliptical hydrofoil. *Journal of Fluid Mechanics* **390**, 1–23.

Brandner, P. A., Lecoffre, Y. & Walker, G. J. 2006 Development of an australian national facility for cavitation research. In *In Sixth International Symposium on Cavitation - CAV 2006*.

Brandner, P. A., Lecoffre, Y. & Walker, G. J. 2007 Design considerations in the development of a modern cavitation tunnel. In *Proceedings of the 16th Australasian Fluid Mechanics Conference, 16AFMC*, pp. 630–637.

Chang, N. A., Choi, J., Yakushiji, R. & Ceccio, S. L. 2012 Cavitation inception during the interaction of a pair of counter-rotating vortices. *Physics of Fluids* **24** (1), 014107.

Doolan, C., Brandner, P., Butler, D., Pearce, B., Moreau, D. & Brooks, L. 2013 Hydroacoustic characterization of the AMC cavitation tunnel. In *In Acoustic 2013, Victor Harbour, Australia*.

Dreyer, M., Decaix, J., Mönch-Alligné, C. & Farhat, M. 2014 Mind the gap: a new insight into the tip leakage vortex using stereo-piv. *Experiments in Fluids* **55** (11), 1849.

Gopalan, S., Katz, J. & Knio, O. 1999 The flow structure in the near field of jets and its effect on cavitation inception. *Journal of Fluid Mechanics* **398**, 1–43.

Gopalan, S., Katz, J. & Liu, H. L. 2002 Effect of gap size on tip leakage cavitation inception, associated noise and flow structure. *Journal of Fluids Engineering* **124** (4), 994–1004.

Guo, Q., Zhou, L. & Wang, Z. 2016 Numerical evaluation of the clearance geometries effect on the flow field and performance of a hydrofoil. *Renewable Energy* **99**, 390–397.

Higashi, S., Yoshida, Y. & Tsujimoto, Y. 2002 Tip leakage vortex cavitation from the tip clearance of a single hydrofoil. *JSME International Journal Series B Fluids and Thermal Engineering* **45** (3), 662–671.

Khoo, M. T., Venning, J. A., Pearce, B. W., Takahashi, K., Mori, T. & Brandner, P. A. 2020 Natural nuclei population dynamics in cavitation tunnels. *Experiments in Fluids* **61** (2), 34.

Laborde, R., Chantrel, P. & Mory, M. 1997 Tip clearance and tip vortex cavitation in an axial flow pump. *Journal of Fluids Engineering* **119** (3), 680–685.

Li, Z., Zheng, X., Liu, Y., Li, Q. & Ji, B. 2016 The effect of end wall boundary layer on matching and corresponding flow control technique for multistage axial compressor. *Proceedings of the Institution of Mechanical Engineers, Part G: Journal of Aerospace Engineering* **230** (12), 2179–2194.

O'Hern, T. J. 1990 An experimental investigation of turbulent shear flow cavitation. *Journal of Fluid Mechanics* **215**, 365–391.

Oweis, G. F. & Ceccio, S. L. 2005 Instantaneous and time-averaged flow fields of multiple vortices in the tip region of a ducted propulsor. *Experiments in Fluids* **38** (5), 615–636.

Ran, B. & Katz, J. 1994 Pressure fluctuations and their effect on cavitation inception within water jets. *Journal of Fluid Mechanics* **262**, 223–263.

Russell, P. S., Barbaca, L., A., Venning. J., Russell, E. S. C., Pearce, B. W. & Brandner, P. A. 2020*a* Cavitation in tip-leakage flows. In *33rd Symposium on Naval Hydrodynamics*.

Russell, P. S, Barbaca, L., Venning, J. A., Pearce, B. W. & Brandner, P. A. 2020*b* Nucleation effects on tip-gap cavitation. In *22nd Australasian Fluid Mechanics Conference (AFMC2020)*, pp. 1–4.

Russell, P. S, Barbaca, L., Venning, J. A., Pearce, B. W. & Brandner, P. A. 2022 The influence of nucleation on cavitation inception in tip-leakage flows. In *34th Symposium on Naval Hydrodynamics*.

Russell, P. S., Barbaca, L., Venning, J. A., Pearce, B. W. & Brandner, P. A. 2023 Influence of nucleation on cavitation inception in tip leakage flows. *Physics of Fluids* **35** (1), 013341.

Smith, S. M., Brandner, P. A., Pearce, B. W., Venning, J. A., Moreau, D. J. & Clarke, D. B. 2021 Steady and unsteady loading on a hydrofoil immersed in a turbulent boundary layer. *Journal of Fluids and Structures* **102**.

Tian, Q. & Simpson, R. 2007*a* Experimental study of tip leakage flow in the linear compressor cascade: Part i - stationary wall. In *45th AIAA Aerospace Sciences Meeting and Exhibit*.

Tian, Q. & Simpson, R. 2007*b* Experimental study of tip leakage flow in the linear compressor cascade: Part ii - effect of moving wall. In *45th AIAA Aerospace Sciences Meeting and Exhibit*.

Wagner, J. H., Dring, R. P. & Joslyn, H. D. 1985*a* Inlet Boundary Layer Effects in an Axial Compressor Rotor: Part II—Throughflow Effects. *Journal of Engineering for Gas Turbines and Power* **107** (2), 381–386.

Wagner, J. H., Dring, R. P. & Joslyn, H. D. 1985*b* Inlet Boundary Layer Effects in an Axial Compressor Rotor: Part I—Blade-to-Blade Effects. *Journal of Engineering for Gas Turbines and Power* **107** (2), 374–380.

Wu, Huixuan, Tan, David, Miorini, Rinaldo L. & Katz, Joseph 2011 Three-dimensional flow structures and associated turbulence in the tip region of a waterjet pump rotor blade. *Experiments in Fluids* **51** (6), 1721–1737.

You, D., Wang, M., Moin, P. & Mittal, R. 2006 Effects of tip-gap size on the tip-leakage flow in a turbomachinery cascade. *Physics of Fluids* **18** (10), 105102.

You, D., Wang, M., Moin, P. & Mittal, R. 2007 Vortex dynamics and low-pressure fluctuations in the tip-clearance flow. *Journal of Fluids Engineering* **129** (8), 1002–1014.

Zhang, B., Liu, B., Mao, X., Wang, H., Yang, Z. & Li, Z. 2022 Interaction mechanism between the tip leakage flow and inlet boundary layer in a highly loaded compressor cascade based on scale-adaptive simulation. *Physics of Fluids* **34** (11), 116112.

Zhang, D., Shi, W., van Esch, B., Shi, L. & Dubuisson, M. 2015 Numerical and experimental investigation of tip leakage vortex trajectory and dynamics in an axial flow pump. *Computers & Fluids* **112**, 61–71.